

Observations of the Ultraviolet-bright Star III-60 in the Globular Cluster NGC 6723

WILLIAM V. DIXON¹

¹*Space Telescope Science Institute, 3700 San Martin Drive, Baltimore, MD 21218, USA*

ABSTRACT

We have analyzed archival far-ultraviolet spectra of the UV-bright star III-60 in the globular cluster NGC 6723 obtained with the Far Ultraviolet Spectroscopic Explorer (FUSE) and the Cosmic Origins Spectrograph (COS). We find that the star’s photospheric parameters (effective temperature $T_{\text{eff}} = 44,800 \pm 1200$, surface gravity $\log g = 4.89 \pm 0.18$, and helium abundance $\log N(\text{He})/N(\text{H}) = -0.84 \pm 0.29$) are consistent with the values derived from its optical spectrum, suggesting that optically-derived values are generally accurate for evolved stars with $T_{\text{eff}} \lesssim 50,000$ K. Relative to the cluster’s RGB stars, III-60 is enhanced in nitrogen and depleted in carbon and oxygen. The star exhibits strong P Cygni profiles in both components of the N V $\lambda 1240$ doublet, but the resonance lines of other species show no evidence of a stellar wind. The star’s effective temperature and luminosity place it on the evolutionary tracks of stars evolving from the blue horizontal branch, but its high mass ($\sim 1.2 M_{\odot}$) indicates that it is the product of a stellar merger. Its helium, carbon, and nitrogen abundances suggest that it is following an evolutionary path similar to that of the low-carbon, intermediate helium-rich hot subdwarfs.

Keywords: stars: abundances — stars: atmospheres — stars: individual (NGC 6723 III-60) — ultraviolet: stars

1. INTRODUCTION

Among the UV-bright stars in the globular cluster NGC 6723—stars that lie above the horizontal branch and to the left of the giant branch in the Hertzsprung–Russell diagram—Menzies (1974) found two “very blue stars,” III-60¹ and IV-9. Moehler et al. (1998) analyzed medium-resolution optical spectra of both stars and identified them as post-early AGB stars, objects that evolved partway up the asymptotic giant branch (AGB) before peeling off to the blue.

Moehler et al. (2019) reanalyzed the spectra, comparing them with grids of non-local thermodynamic equilibrium (non-LTE) line-blanketed model atmospheres and non-LTE synthetic spectra. Using models with $[M/H] = -1.1$ and scaled-solar abundances, they derived $T_{\text{eff}} = 43,000 \pm 1400$ K, $\log g = 4.72 \pm 0.14$, and $\log N(\text{He})/N(\text{H}) = -1.19 \pm 0.14$ for the star III-60. For many of the stars in their sample, Moehler et al. could

not fit the H, He I, and He II lines simultaneously, because the observed He I lines were weaker than predicted, while the H and He II lines were stronger.

Latour et al. (2015) observed a similar behavior in the spectrum of the hot subdwarf O star BD+28°4211. Suspecting that the stellar atmosphere was affected by opacities not included in the models, they found that model atmospheres with $[M/H] = +1.0$ were better able to fit the star’s H and He lines and to reproduce the stellar parameters derived from far-ultraviolet (FUV) observations. Using similar metal-enriched models, Moehler et al. derived $T_{\text{eff}} = 42,300 \pm 1400$, $\log g = 4.80 \pm 0.12$, and $\log N(\text{He})/N(\text{H}) = -1.13 \pm 0.12$ for III-60 in NGC 6723.

Because the parameters derived from the $[M/H] = -1.1$ and $+1.0$ models agree within the uncertainties, we should have a good handle on the temperature of this star. There is, however, one more consideration. The spectrum of Y543 in NGC 6121 was also reanalyzed by Moehler et al. (2019). Models with $[M/H] = -1.16$ yield $T_{\text{eff}} = 54,900 \pm 2000$, $\log g = 5.62 \pm 0.14$, and $\log N(\text{He})/N(\text{H}) = -1.25 \pm 0.10$, while those with $[M/H] = +1.0$ yield $T_{\text{eff}} = 56,500 \pm 1800$, $\log g = 5.71 \pm 0.12$, and $\log N(\text{He})/N(\text{H}) = -1.16 \pm 0.10$. Again, the parameters agree within the uncertainties, but Dixon et al. (2017)

Corresponding author: William V. Dixon
dixon@stsci.edu

¹ SIMBAD refers to this star as NGC 6723 360. Its coordinates are 18:59:29.0 –36:40:49.0 (Moehler et al. 1998).

found that model fits to the CNO lines in the star’s HST/COS spectrum require $T_{\text{eff}} \sim 72,000$ K, an effective temperature considerably higher than that derived from its optical spectrum.

To investigate whether a similar phenomenon is at work in III-60, we analyze archival FUV spectra spanning wavelengths from about 1765 \AA to the Lyman limit. In Section 2, we present our data. In Section 3, we discuss our atmospheric models and use them to derive stellar parameters and abundances. In Section 4, we discuss the wind profiles seen in the star’s N V $\lambda 1240$ resonance lines. In Section 5, we discuss our results and consider the evolutionary history of the star. We summarize our conclusions in Section 6.

2. OBSERVATIONS AND DATA REDUCTION

The star III-60 was observed with both the Far Ultraviolet Spectroscopic Explorer (FUSE) and the Cosmic Origins Spectrograph (COS) aboard the *Hubble Space Telescope*. Observational details are presented in Table 1.

2.1. FUSE Data

FUSE provides medium-resolution spectroscopy from 1187 \AA to the Lyman limit (Moos et al. 2000; Sahnou et al. 2000). The star III-60 was observed through the $30'' \times 30''$ LWRS aperture. The data were reduced using v3.2.2 of CalFUSE, the standard data-reduction pipeline software (Dixon et al. 2007), and retrieved from the Mikulski Archive for Space Telescopes (MAST). For each FUSE channel, the extracted spectra from all exposures are shifted to a common wavelength scale, weighted by exposure time, and combined into a single file. Because each channel has a unique line-spread function, we prefer not to combine the spectra from multiple channels, instead using only the spectrum from the channel with the highest signal-to-noise ratio (S/N). In this case, in order to maximize the S/N, we combine spectra from the SiC1 and SiC2 channels for the wavelength region $917\text{--}988 \text{ \AA}$ and from the LiF1 and LiF2 channels in the region $1180\text{--}1190 \text{ \AA}$. We exclude the data from the SiC2 channel, exposures 1 and 2, of observation A1080201 and all of the Side 2 data of exposure D1570201, because the star had drifted out of the aperture. The S/N of the resulting spectrum is ~ 7 per 0.05 \AA resolution element in the SiC band ($900\text{--}1000 \text{ \AA}$) and ranges from 10 to 15 in the LiF band ($1000\text{--}1187 \text{ \AA}$). The FUSE wavelength calibration is reasonably accurate, but small offsets of the target within the LWRS aperture can introduce a zero-point offset in the wave-

length scale. To place the data on an absolute wavelength scale, we shift the spectrum so that the velocities of its interstellar lines match those of the COS spectrum, which are heliocentric. The FUSE data used in this work are available at [10.17909/4jy0-pr10](https://doi.org/10.17909/4jy0-pr10).

2.2. COS Spectroscopy

COS enables high-sensitivity, medium- and low-resolution spectroscopy in the $1150\text{--}3200 \text{ \AA}$ wavelength range (Green et al. 2012). The star was observed with COS using the G130M and G160M gratings, each at multiple central-wavelength settings. Because the CALCOS pipeline does not automatically combine exposures taken with different central wavelengths, we retrieved the fully-reduced and combined G130M and G160M spectra from the Hubble Advanced Spectral Product (HASP; Debes et al. 2024) program, available from MAST. The S/N per resolution element varies between 20 and 35 in the G130M spectrum. In the G160M spectrum, the S/N falls monotonically from ~ 35 at 1400 \AA to ~ 10 at 1750 \AA .

3. ANALYSIS

3.1. Interstellar Medium

The FUV spectrum of III-60 includes a variety of interstellar absorption features. In the FUSE bandpass, molecular hydrogen is the dominant species, while high-ionization species are prominent at longer wavelengths. Synthetic interstellar absorption spectra are computed using software written at the University of California, Berkeley, by M. Hurwitz and V. Saba. Given the column density, Doppler broadening parameter, and velocity of each component, the program computes a Voigt profile for each absorption feature and produces a high-resolution spectrum of optical depth versus wavelength. Wavelengths, oscillator strengths, and other atomic data are taken from Morton (2003). We fit these features by eye, which is sufficient for our needs.

Lehner et al. (2012) report the detection of absorption from C II $\lambda 1334$ and Si II $\lambda\lambda 1260, 1526$ with $v_{\text{LSR}} \sim -90 \text{ km s}^{-1}$ in the COS spectrum of III-60, which they attribute to a high-velocity cloud (HVC) along the line of sight. Their estimate of the stellar velocity is -101 km s^{-1} , so stellar features are blue-shifted with respect to both the HVC and the local interstellar medium (ISM). We have incorporated these features into our ISM model. The question of whether any HVC absorption lines are blended with stellar features, complicating our estimate of the star’s metal abundances, is addressed in Section 3.5.

3.2. Model Atmospheres

Table 1. Summary of FUSE and COS Observations

Instrument	Grating	Cenwave (Å)	Wavelength Range (Å)	$R \equiv \lambda/\Delta\lambda$	Exp. Time (s)	Obs. Date	Data ID	P.I.
FUSE	905–1187	20,000	5,365	2000 May 15	A1080201	Dixon
					13,537	2004 Sep 15	D1570201	Dixon
COS	G130M	1291	1137–1433	15,000–21,000	390	2010 Mar 4	LB3Z11010	Lehner
	G130M	1327	1174–1471	15,000–21,000	310	2010 Mar 4	LB3Z11020	Lehner
	G160M	1577	1388–1754	15,000–22,000	410	2010 Mar 4	LB3Z11030	Lehner
	G160M	1589	1400–1765	15,000–22,000	490	2010 Mar 4	LB3Z11040	Lehner

We compute non-LTE stellar-atmosphere models using version 208 of the program TLUSTY (Hubeny & Lanz 1995). We employ atomic models similar to those used by Lanz & Hubeny (2003) to compute their grid of O-type stars. We begin by adopting the stellar parameters derived by Moehler et al. (2019), $T_{\text{eff}} = 43,000 \pm 1400$, $\log g = 4.72 \pm 0.14$, and $\log N(\text{He})/N(\text{H}) = -1.19 \pm 0.14$, using models with $[M/\text{H}] = -1.1$ and scaled-solar abundances. Given a model atmosphere, we compute a synthetic spectrum using version 54 of the program SYNSPEC (Hubeny 1988). For the FUSE data, synthetic spectra are convolved with a Gaussian of $\text{FWHM} = 0.06 \text{ \AA}$ to match the FUSE line-spread function. For the COS spectrum, we employ the tabulated line-spread functions appropriate for data obtained at Lifetime Adjustment Position #1, which are available from the COS website. We multiply the synthetic spectrum by a Fitzpatrick (1999) extinction curve assuming $E(B-V) = 0.05$ (Harris 1996, 2010), extrapolated to the Lyman limit, and the ISM absorption model described above. Finally, we scale the model to reproduce the continuum in a nearby (apparently) line-free region in the observed spectrum.

Given a grid of synthetic spectra, prepared as described above, our fitting routine linearly interpolates among them—in one, two, or three dimensions, as appropriate—determining the best fit to the data via chi-squared minimization. The uncertainties quoted for parameters derived from individual line fits are 1σ errors computed from the covariance matrix returned by the fitting routine; we refer to these as statistical errors.

Continuum placement is the dominant uncertainty in our fits. Weak absorption lines not included in our model may depress the apparent continuum. Allowing our fitting routines to scale the model to the mean level of the “pseudo-continuum” thus underestimates the true continuum level. To estimate the uncertainty inherent in our continuum estimate, we perform each fit twice, once with the model continuum fixed as described and

again with the model scaled by a factor of 0.97. The difference in the two abundances is an estimate of the systematic error in our abundance estimates. We add this term and the statistical error in quadrature to compute our final error for a single absorption feature. In most cases, the continuum uncertainty is the dominant contributor to the final error.

3.3. Effective Temperature and CNO Abundances

Following Dixon (2024), we use the absorption features of multiple ionization states of CNO to derive the star’s effective temperature. Consider the middle panel of Fig. 1. Using a series of models with $T_{\text{eff}} = 43,000 \text{ K}$ and $\log N(\text{N})/N(\text{H})$ between -4.5 and -2.5 , we fit the N III $\lambda 979$ feature to determine the nitrogen abundance. We repeat using models with temperatures increasing in steps of 1000 K to 47,000 K. The resulting nitrogen abundances are plotted as dark blue points and connected by a low-order polynomial (evaluated at 10 K intervals). Vertical bars represent the uncertainties returned by the fitting routine. As the temperature rises, the fraction of nitrogen in the form of N III falls, requiring a higher nitrogen abundance to reproduce the observed feature. We repeat this procedure for a handful of other N III and N IV lines.

We repeat the process for C and O (top and bottom panels of Fig. 1). Note that the hottest available oxygen models have temperatures of 45,500 K; hotter models fail to converge. We exclude from consideration features that yield wildly discrepant abundances, as well as those that yield abundances with error bars so large that they provide no useful constraints. We see that the curves cross at a temperature near 45,000 K. To combine these results in a quantifiable way, we compute the error-weighted mean abundance and the error-weighted standard deviation as a function of temperature for each element. The mean abundance is plotted as a dotted line

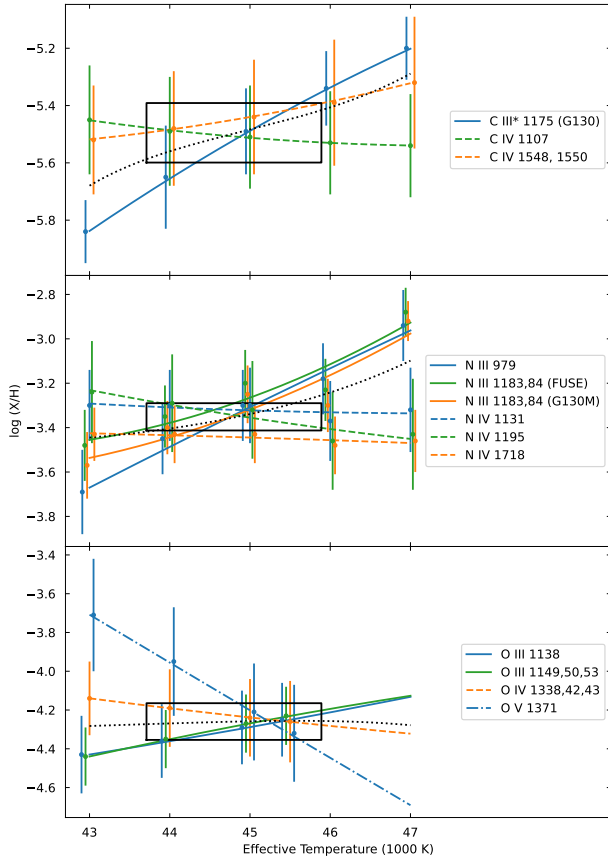


Figure 1. Deriving the effective temperature and CNO abundance. Points with error bars represent the abundance derived from model fits to each absorption feature. Solid and dashed lines are low-order polynomial fits to the measured points. Dotted lines represent the weighted mean of the measured abundances, computed at 10 K intervals. The black box in each panel denotes the allowed ranges of temperature and abundance, as described in the text.

in each panel. At each temperature step, we compute

$$\chi^2 = \sum \left\{ [y_i - y(x_i)]^2 / \sigma_i^2 \right\},$$

where y_i is the abundance derived from a single feature (or group of features; solid or dashed line), $y(x_i)$ is the mean abundance (dotted line), σ_i is the uncertainty in the derived abundance (vertical bars), and the summation is taken over the 13 abundance curves plotted in Fig. 1. χ^2 has a minimum at $T_{\text{eff}} = 44,840$ K. Our lower limit to the temperature is $T_{\text{eff}} = 43,710$ K, set by the point at which χ^2 rises by 4.72 relative to its minimum. This choice of $\Delta\chi^2$ is strictly correct for a model with four interesting parameters (one temperature and three abundances) if all errors are normally distributed (Press et al. 1989). For each element, our best-fit abundance is the error-weighted mean value (computed above) at the best-fit temperature. The abundance uncertainty is

the larger of the error-weighted standard deviation or the uncertainty in the weighted mean. The black box in each panel illustrates the best-fit effective temperature and elemental abundance and their uncertainties. Our derived stellar parameters are presented in Table 2 and abundances in Table 3.

3.4. Surface Gravity and Helium Abundance

To determine the surface gravity and helium abundance of III-60, we fit a small grid of models to the star’s He II $\lambda 1640$ line. The models have $T_{\text{eff}} = 44,800$ K; $\log g = 4.50, 4.75, \text{ and } 5.00$; and $\log N(\text{He})/N(\text{H}) = -0.5, -1.0, \text{ and } -1.5$. Our best-fit model has $\log g = 4.89 \pm 0.18$ and $\log N(\text{He})/N(\text{H}) = -0.84 \pm 0.29$. The He II feature, along with two of our models, is presented in Fig. 2. We see that increasing the surface gravity increases the depth of the He II line. Increasing the He abundance has the same effect, so we cannot place tight constraints on the two parameters simultaneously, as indicated by their relatively large error bars. Note that the line core, which is both broader and deeper than our models, is excluded from the fit.

Formally, our best-fit surface gravity and helium abundance are consistent with the values $\log g = 4.80 \pm 0.12$ and $\log N(\text{He})/N(\text{H}) = -1.13 \pm 0.12$ determined from the star’s optical spectrum (Moehler et al. 2019); however, the fact that we derive larger values for both parameters suggests that the He II $\lambda 1640$ line is stronger than its optical counterparts. Indeed, fixing the surface gravity at its optically-derived value yields a helium abundance $\log N(\text{He})/N(\text{H}) = -0.69$. The He II $\lambda 958$ line is also quite strong, but its low S/N precludes its use in this analysis. In the rest of this paper, we will adopt the FUV-derived values of the surface gravity and helium abundance while keeping in mind the uncertainties in both parameters.

Are the new helium abundance and surface gravity sufficiently different from our initial models that we must recompute the temperature and CNO abundance? To find out, we generate a grid of models with $T_{\text{eff}} = 45,000$ K, $\log g = 4.89$, $\log N(\text{He})/N(\text{H}) = -0.84$, and $\log N(\text{N})/N(\text{H})$ ranging from -2.5 to -4.5 . Fitting this grid to our set of nitrogen lines yields $\log N(\text{N})/N(\text{H}) = -3.35 \pm 0.04$. Fits to our initial set of models with the same temperature yields $\log N(\text{N})/N(\text{H}) = -3.30 \pm 0.07$. The difference is small enough that we need not revisit our earlier computations.

3.5. Metal Abundances

As mentioned above, some of the star’s CNO lines yield abundances that are discrepant from others of their

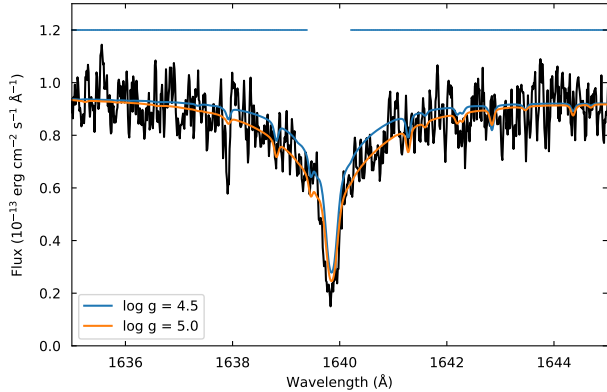


Figure 2. He II $\lambda 1640$ feature in the spectrum of III-60 in NGC 6723. For this figure, the data are smoothed by three pixels. Synthetic spectra with $\log g = 4.5$ and 5.0 are overplotted. Both models have $T_{\text{eff}} = 44,800$ K and $\log N(\text{He})/N(\text{H}) = -0.84$. Blue bars indicate the spectral regions included in our fit.

Table 2. Stellar Parameters

Parameter	Value
T_{eff} (K)	$44,800 \pm 1100$
$\log g$ [cm s^{-2}]	4.89 ± 0.18
$\log N(\text{He})/N(\text{H})$	-0.84 ± 0.29
R_*/R_{\odot}	0.65 ± 0.01
M_*/M_{\odot}	1.18 ± 0.49
$\log(L_*/L_{\odot})$	3.18 ± 0.05

species or whose error bars are so large that they provide no constraint on the effective temperature. To give a sense of these features, we present in Table A1, found in the Appendix, abundances derived from a number of CNO features, including several that are not included in Fig. 1.

Five other elements, Si, P, S, Fe, and Ni, exhibit absorption lines in the spectrum of III-60. We derive their abundances by fitting synthetic spectra to the features listed in Table A2, also found in the Appendix. We fit each line or group of lines separately. For each of these elements, the final abundance and its uncertainty represent the mean and standard deviation of our individual measurements. Results are presented in Table 3 and plotted in Fig. 3.

Notes on individual elements follow.

Carbon: The two components of the C IV $\lambda\lambda 1548, 1550$ resonance doublet are strong in both the stellar photosphere and the local ISM. If significant C IV were present in the HVC reported by Lehner et al.

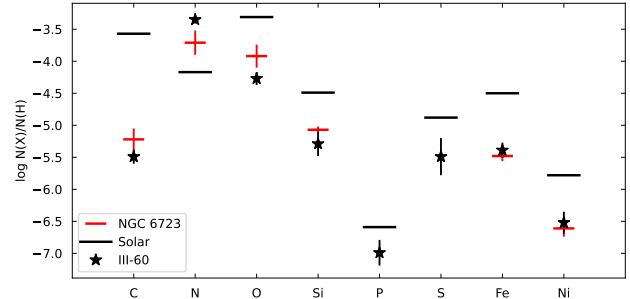


Figure 3. Photospheric abundances of III-60 (stars), NGC 6723 (red lines), and the solar photosphere (black lines). See Table 3 for references.

(2012), its features would be blended with the corresponding stellar lines. To minimize interstellar contamination, we fit only the blue wing of each component of the doublet. These lines yield carbon abundances similar to those of the star’s other C IV features, suggesting that any contamination is minor.

Nitrogen: The N IV $\lambda 1718$ feature is quite strong, but its blue wing is blended with a couple of stellar features, probably due to Fe V, that are not reproduced by our model. We fit only the red wing of the line. We do not attempt to fit the N V $\lambda\lambda 1238, 1242$ resonance doublet, as both components are hopelessly entangled with the P Cygni profiles discussed in Section 4.

Silicon: The discussion of the C IV $\lambda\lambda 1548, 1550$ lines also applies to the Si IV $\lambda\lambda 1393, 1402$ resonance doublet.

Phosphorus: If significant P V were present in the HVC, then the stellar resonance features at 1117 and 1128 Å could be contaminated. Furthermore, our models predict that P IV $\lambda 1033$ is blended with an O III feature, while P V $\lambda 1117$ is blended with N IV. Nevertheless, the scatter in the abundance values derived from the four P lines listed in Table 3 is relatively small, so we adopt their mean as the stellar value.

Iron: There are hundreds of iron lines in the FUV spectrum of III-60, most due to Fe V. Instead of fitting individual features, we divide the G160M spectrum into several short segments, mask the ISM features and all stellar features that are not due to iron, and fit our model spectra to each segment.

Nickel: In most cases, we fit individual nickel lines. One exception is the region 1265–1268 Å, which contains several strong Ni V features. We fit our model spectra to this segment, just as we did for the iron lines.

4. STELLAR WIND

The FUV spectra of many hot post-AGB stars exhibit wind features from a variety of species (e.g., Guerrero & De Marco 2013). Fig. 4 presents the resonance

Table 3. Photospheric Abundances

Species	III-60	NGC 6723	Sun
He	-0.84 ± 0.29	...	-1.07 ± 0.01
C	-5.50 ± 0.10	-5.22 ± 0.17	-3.57 ± 0.05
N	-3.35 ± 0.06	-3.71 ± 0.19	-4.17 ± 0.05
O	-4.26 ± 0.09	-3.92 ± 0.18	-3.31 ± 0.05
Si	-5.29 ± 0.19	-5.07 ± 0.05	-4.49 ± 0.03
P	-6.99 ± 0.20	...	-6.59 ± 0.03
S	-5.49 ± 0.29	...	-4.88 ± 0.03
Fe	-5.39 ± 0.12	-5.48 ± 0.08	-4.50 ± 0.04
Ni	-6.52 ± 0.17	-6.61 ± 0.13	-5.78 ± 0.04

NOTE—Abundances relative to hydrogen: $\log N(X)/N(H)$. Cluster values for C and N from Gerber et al. (2019), for O, Si, and Fe from Rojas-Arriagada et al. (2016), and for Ni from Crestani et al. (2019). Solar values from Asplund et al. (2009).

lines of O VI $\lambda 1034$, N V $\lambda 1240$, Si IV $\lambda 1397$, and C IV $\lambda 1550$. Only the N V $\lambda 1240$ doublet shows evidence of a wind. Its blue component exhibits a P Cygni absorption trough extending about 1100 km s^{-1} blueward of the photospheric line and reaching depths of about 60% below the continuum. Its red component exhibits redshifted emission. The continuum for the other resonance lines is flat; no broad absorption is observed.

Chayer et al. (2015) found that, like III-60 in NGC 6723, the UV-bright star vZ 1128 in M3 (NGC 5272) exhibits P Cygni profiles in both components of the N V $\lambda 1240$ doublet, but in no other absorption lines. They performed a simple calculation to show that the low abundance of C and Si (relative to N), combined with the tiny fraction of these elements in the form of C IV and Si IV, suggest that the optical depth of their wind features would be only a few percent that of N V. The same argument explains the absence of O VI, S IV, and C IV wind lines in the spectrum of III-60.

5. DISCUSSION

5.1. Cluster Membership

Before comparing III-60 with other members of NGC 6723, we should confirm that it is a cluster member. The star lies about $3'$ from the cluster center (Menzies 1974), and its radial velocity, $v_{\text{LSR}} = -101 \pm 10 \text{ km s}^{-1}$ (Lehner et al. 2012), is consistent with the cluster mean of $v_{\text{LSR}} = -88.3 \pm 3.6 \text{ km s}^{-1}$ (Harris 1996, 2010). Vasiliev & Baumgardt (2021) use data from *Gaia* Early Data Release 3 (EDR3; Gaia Collaboration et al. 2016, 2021) to study the kinematic properties of 170 Milky Way globular clusters. They provide catalogues of all

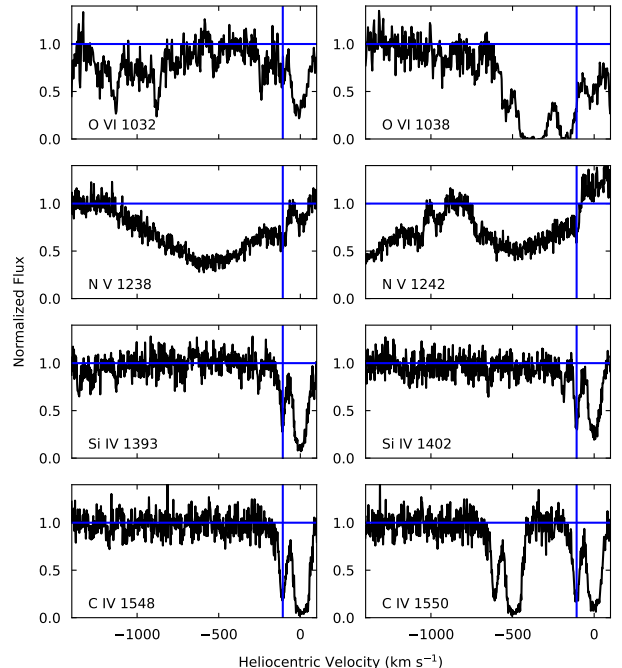


Figure 4. Normalized profiles of the resonance doublets observed in the spectrum of III-60. The horizontal line corresponds to the normalized continuum. The vertical line indicates the radial velocity of the star. Except for the resonance lines, all of the features are interstellar.

Gaia sources in the field of each cluster. They estimate a membership probability of 0.997 for III-60. We conclude that the star is a cluster member.

5.2. Photospheric Abundances

Table 3 and Fig. 3 compare the measured abundances of III-60 with the average of the cluster’s RGB stars and with the sun. The star’s He abundance is super-solar, but the uncertainty is large. The star is enhanced in N and depleted in C and O, a pattern generally attributed to hydrogen burning via the CNO cycle. The star’s Si, Fe, and Ni abundances are consistent with the cluster values. Any evolutionary scenario proposed for III-60 must be able to explain this abundance pattern. Note that we have adopted the Fe abundance of Rojas-Arriagada et al. (2016), who found $[\text{Fe}/\text{H}] = -0.98 \pm 0.08$, but the cluster abundance is somewhat uncertain. Recent spectroscopic estimates range from $[\text{Fe}/\text{H}] = -0.93 \pm 0.05$ (Crestani et al. 2019) to $[\text{Fe}/\text{H}] = -1.22 \pm 0.08$ (Gratton et al. 2015).

5.3. Stellar Mass and Luminosity

We can derive a star’s radius, and from this its mass and luminosity, by comparing its observed and predicted fluxes. The spectral irradiance of III-60, as reported in *Gaia* Data Release 3 (DR3; Gaia Collaboration et al.

2016, 2023), is $G = 15.552 \pm 0.003$ mag. (The star is designated Gaia DR3 6730904559676428544.) We generate a synthetic spectrum using our best-fit model, scaled by a Fitzpatrick (1999) extinction curve with $R_V = 3.1$ and $E(B - V) = 0.05$ (Harris 1996, 2010). We compute synthetic stellar magnitudes using the recipe provided in Riello et al. (2021). The ratio between the observed and model fluxes is $\phi = (3.89 \pm 0.01) \times 10^{-23}$.

In the synthetic spectra generated by SYNSPEC, the flux is expressed in terms of the flux moment, H_λ . If the star’s radius and distance are known, then the scale factor required to convert the model spectrum to the flux at earth is $\phi = 4\pi(R_*/d)^2$ (Kurucz 1979). Using a combination of Gaia EDR3, *HST*, and literature data, Baumgardt & Vasiliev (2021) derive a distance to NGC 6723 of 8.267 ± 0.100 kpc. Adopting this distance and our scale factor, we derive a stellar radius R_*/R_\odot of 0.65 ± 0.01 . Applying our adopted surface gravity ($\log g = 4.89 \pm 0.18$), we find that the stellar mass M_*/M_\odot is 1.18 ± 0.49 . Finally, combining the stellar radius with our best-fit effective temperature ($T_{\text{eff}} = 44,800 \pm 1100$ K), we derive a stellar luminosity $\log L_*/L_\odot$ of 3.18 ± 0.05 . (The uncertainties on these values are calculated via simple propagation of errors.)

While a stellar mass of $1.18 M_\odot$ greatly exceeds the $0.53 \pm 0.01 M_\odot$ that one would expect for a soon-to-be white dwarf in a globular cluster (Kalirai et al. 2009), the value seems secure. Adopting the Gontcharov et al. (2023) correction for differential reddening across the cluster yields $E(B - V) = 0.069$ and $M_*/M_\odot = 1.25$. Adopting the scale factor from our fits to the star’s G160M spectrum ($\phi = 3.31 \times 10^{-23}$) yields $M_*/M_\odot = 1.00$. From the star’s optical spectrum, Moehler et al. (2019) derived a mass of $1.19 \pm 0.3 M_\odot$ (the error bar is from their Fig. 5).

5.4. Opacity Effects

One motivation of this study is to determine whether the star’s optical hydrogen and helium features yield stellar parameters, particularly effective temperature, consistent with those derived from the ionization balance of the star’s FUV lines. In this case, the answer is yes, but careful consideration of our results provides interesting insights into opacity effects in stellar atmospheres.

The discrepancy between the optical and UV-derived effective temperatures may be a symptom of the Balmer-line problem (Napiwotzki et al. 1993; Werner et al. 1996), the inability of models to reproduce simultaneously the full set of Balmer lines with a single set of stellar parameters (T_{eff} and $\log g$). Apparently, there are sources of opacity in the atmospheres of hot stars that

are not included in our models. For only a handful of globular-cluster stars are both optical and UV temperatures available. We do not find a significant discrepancy in III-60, for which $T_{\text{eff}} \sim 45,000$ K. Latour et al. (2017) found that, while the optically-derived temperatures of subdwarf O (sdO) stars in ω Cen are about 50,000 K, the UV-derived temperatures are closer to 60,000 K. The UV-bright star Y453 in M4 (NGC 6121) yields an optical temperature of 56,500 K (Moehler et al. 2019) and a UV temperature of 72,000 K (Dixon et al. 2017). If effective temperature is the only relevant parameter (which is unlikely), then the discrepancy appears in stars hotter than about 50,000 K.

Another source of opacity is the diffusion of heavy elements into the stellar atmosphere. The abundance ratios of these elements represent an equilibrium among several physical processes, including radiative levitation, which injects heavy elements into the atmosphere from below; gravitational settling, which pulls them from the atmosphere into the interior; and the stellar wind, which ejects them into the ISM.

The abundance anomalies seen in some sdO stars (which have $T_{\text{eff}} > 40,000$ K and $\log g = 5.0$ – 6.5), particularly enrichments in iron-group and trans-iron elements, are attributed to diffusion processes in the stellar atmosphere (Heber 2016). We have seen that the photospheric abundances of III-60 are consistent with the cluster values (though its CNO abundances have clearly been modified). With stellar parameters similar to those of sdO stars, III-60 might show abundance anomalies if not for its stellar wind. Diffusion velocities in stellar atmospheres may reach about 1 cm s^{-1} in the line-forming region. When the wind velocity is significantly greater than the diffusion velocity, the accumulation of material lifted from below is impossible (Michaud et al. 2015, pp. 134–135). We can compare III-60 with the Y453, whose abundances are clearly influenced by diffusion processes; that star has $T_{\text{eff}} = 72,000$ K, $\log g = 5.7$, and no detectible wind (Dixon et al. 2017).

5.5. Evolutionary Status

The effective temperature and luminosity of III-60 place it on the evolutionary tracks of stars evolving from the blue horizontal branch (BHB; Moehler et al. 2019). NGC 6723 has an extended HB, well populated on both sides of the RR Lyrae instability strip, so a BHB origin for III-60 would be reasonable if its mass were roughly half the measured value. Instead, the star’s high mass suggests that III-60 is the product of a stellar merger. We consider several possibilities.

The simplest explanation is that the star is a blue straggler, still on the main sequence, but a main-

sequence star of this temperature would have a mass of $120 M_{\odot}$ and a radius of $15 R_{\odot}$ (Cox 2000). We can also exclude the possibility that the star is a blue straggler that evolved through the AGB stage without undergoing further interactions with its neighbors. Such stars might have main-sequence masses of 2 or $3 M_{\odot}$, but the stellar-evolution models of Miller Bertolami (2016) predict that they evolve into objects with final masses of 0.6 to $0.8 M_{\odot}$, lower than is observed. Furthermore, in the post-AGB phase, these stars are enhanced in carbon and depleted in nitrogen (a result of third dredge-up on the AGB), while III-60 is depleted in carbon and enhanced in nitrogen.

III-60 must be the result of a stellar merger that occurred at a later evolutionary stage. Perhaps the star is related to the hot subdwarf stars, some of which may be the products of the merger of two helium white dwarfs (Webbink 1984) or of a helium white dwarf and a low-mass main-sequence companion (Clausen & Wade 2011). Luo et al. (2024) derived the abundances of He, C, and N in 210 He-rich hot subdwarfs included in both the Gaia DR3 and LAMOST DR7 (Luo et al. 2022) data sets. They distinguished between extreme helium-rich (eHe) stars, with $\log N(\text{He})/N(\text{H}) > 0$, and intermediate helium-rich (iHe) stars, with $-1 < \log N(\text{He})/N(\text{H}) < 0$. Fig. 5, reproduced from their paper, shows correlations between the carbon (upper panel) and nitrogen abundance (lower panel) and the helium abundance. In both panels, the dashed lines represents the trends identified by Németh et al. (2012).

Luo et al. (2024) identified three groups of stars in the C-He plane: eHe stars (blue points) that follow the Németh et al. (2012) relation, iHe stars (green points) that lie above the Németh et al. relation, and iHe and eHe stars that fall on a shallower relation, marked in Fig. 5 with a solid line. Luo et al. suggested that these three groups may represent three different mechanisms for the production of hot subdwarfs. In the N-He plane, all of the stars fall on the Németh et al. relation. The abundances of III-60 (black star) place it among the low-carbon iHe stars.

How does the mass of III-60 compare with those of the hot subdwarfs? In Fig. 6, we plot stellar mass as a function of helium abundance. In this figure, we include the helium-weak stars (wHe; magenta points), with $-2.2 < \log N(\text{He})/N(\text{H}) < -1.0$, from the Luo et al. (2024) sample. We see that, while most hot subdwarfs have masses near $0.5 M_{\odot}$, masses near $1 M_{\odot}$ are not unusual, even among stars with sub-solar abundance. We conclude that III-60 may be the product of an evolutionary path similar to that of the low-carbon iHe hot subdwarfs.

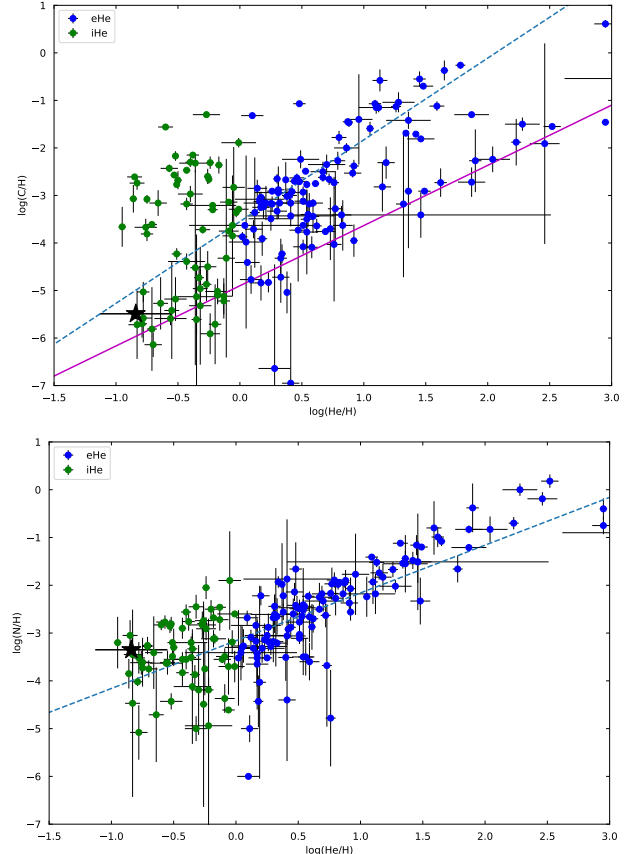


Figure 5. Abundance correlations of hot subdwarf stars. Top panel: carbon abundance vs. helium abundance. Bottom panel: nitrogen abundance vs. helium abundance. Extreme helium-rich (eHe) stars are plotted in blue, intermediate helium-rich (iHe) stars in green. III-60 is in black. Stellar data are from Luo et al. (2024). Dashed lines represent the best-fit trends of Németh et al. (2012). Solid line is a trend identified by Luo et al.

Note: We derive stellar masses for the Luo et al. (2024) sample by converting their Gaia G-band magnitudes to V-band magnitudes using the relation provided in Table 5.9 of the Gaia DR3 Documentation. We convert from observed to bolometric magnitudes using the dust maps of the Planck Collaboration et al. (2014) and the bolometric corrections of Flower (1996) as amended by Torres (2010). The distance, effective temperature, and surface gravity of each star are taken from the Luo et al. catalog.

6. CONCLUSIONS

We have analyzed archival FUV spectra of the hot UV-bright star III-60 in the globular cluster NGC 6723. We find that the star’s photospheric parameters (effective temperature, surface gravity, and helium abundance) are consistent with the values derived from its

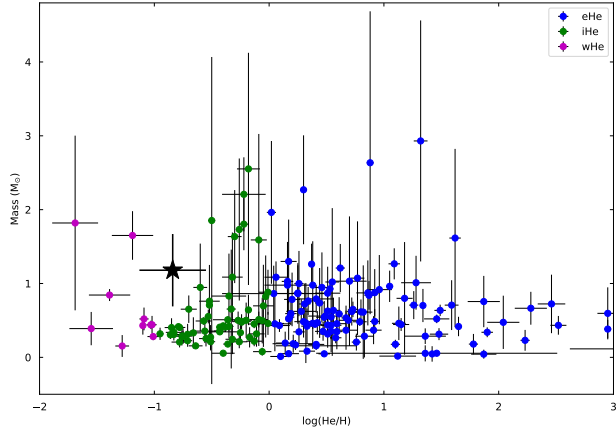


Figure 6. Stellar mass vs. helium abundance. Extreme helium-rich (eHe) stars are plotted in blue, intermediate helium-rich (iHe) stars in green, and helium-weak (wHe) stars in magenta. III-60 is black. Stellar data are from Luo et al. (2024).

optical spectrum, suggesting that optically-derived values are generally accurate for evolved stars with $T_{\text{eff}} \lesssim 50,000$ K. Relative to the cluster’s RGB stars, III-60 is enhanced in nitrogen and depleted in carbon and oxygen. The star exhibits strong P Cygni profiles in both components of the N V $\lambda 1240$ doublet, but the resonance lines of other species show no evidence of a stellar wind. The star’s effective temperature and luminosity place it on the evolutionary tracks of stars evolving from the BHB, but its high mass suggests that it is the product of a stellar merger. Its helium, carbon, and nitrogen abundances suggest that it is traversing an evolutionary path similar to that of the low-carbon, intermediate helium-rich hot subdwarfs.

The author would like to thank P. Chayer for many helpful discussions. This work has made use of NASA’s Astrophysics Data System (ADS); the SIMBAD database, operated at CDS, Strasbourg, France; the Mikulski Archive for Space Telescopes (MAST), hosted at the Space Telescope Science Institute, which is operated by the Association of Universities for Research in Astronomy, Inc., under NASA contract NAS5-26555; and data from the European Space Agency (ESA) mission Gaia (<https://www.cosmos.esa.int/gaia>), processed by the Gaia Data Processing and Analysis Consortium (DPAC; <https://www.cosmos.esa.int/web/gaia/dpac/consortium>). Funding for the DPAC has been provided by national institutions, in particular the institutions participating in the Gaia Multilateral Agreement. Publication of this work is supported by the STScI Director’s Discretionary Research Fund.

Facilities: FUSE, HST(COS)

APPENDIX

A. SELECTED FEATURES IN THE SPECTRUM OF III-60

Table A1. Selected CNO Features

Ion	λ_{lab} (Å)	$\log gf$	E_l (cm^{-1})	Abundance	Grating
C III	1175.665 ^a	0.39	52419.400	-5.81 ± 0.09	FUSE
	1175.665 ^a	0.39	52419.400	-5.49 ± 0.15	G130M
C III	1247.383	-0.31	102352.040	-6.06 ± 0.29	G130M
C IV	1107.591	0.03	320050.090	-5.51 ± 0.18	FUSE
	1107.930	0.29	320081.692	...	
	1168.847	0.61	324879.804	-6.35 ± 0.30	FUSE
	1168.990	0.77	324890.316	...	
	1168.847	0.61	324879.804	-5.20 ± 0.15	G130M
	1168.990	0.77	324890.316	...	
	1548.195	-0.42	0.000	-5.44 ± 0.20	G160M
	1550.772	-0.72	0.000	...	
	N III	979.876 ^a	0.15	101027.0	-3.40 ± 0.18
1005.993		-0.81	131004.300	-3.13 ± 0.16	
1006.036		-1.12	131004.300	...	
1182.971		-0.924	145875.700	-3.33 ± 0.16	
1183.032		-0.608	145875.700	...	
1184.514		-0.212	145985.800	...	
1184.574		-0.915	145985.800	...	
1182.971		-0.924	145875.700	-3.39 ± 0.13	G130M
1183.032		-0.608	145875.700	...	
1184.514		-0.212	145985.800	...	
N IV	1131.488	-0.47	406022.802	-3.33 ± 0.16	FUSE
	1132.021	-1.05	405971.587	...	
	1132.225	-1.17	405987.486	...	
	1132.677	-0.95	406022.802	...	
	1132.944	-1.05	405987.486	...	
	1133.121	-0.41	377284.782	...	
	1135.252	-0.63	377284.782	...	
	1136.273	-1.11	377284.782	...	
	1195.567	-0.58	420049.619	-3.37 ± 0.24	G130M
	1195.732	-1.06	420049.619	...	
	1195.852	-0.31	420058.003	...	
	1718.550	-0.289	130693.900	-3.27 ± 0.13	G160M

Table A1 *continued*

Table A1 (*continued*)

Ion	λ_{lab} (\AA)	$\log gf$	E_l (cm^{-1})	Abundance	Grating
O III	1138.535	-0.76	210461.787	-4.29 ± 0.19	FUSE
	1149.634	-1.08	197087.711	-4.27 ± 0.15	
	1150.884	-0.60	197087.711	...	
	1153.775	-0.38	197087.711	...	
	1196.753	-0.35	294002.875	-4.22 ± 0.33	G130M
	1197.239	-0.19	294223.069	...	
	1197.331	-0.52	293866.497	...	
O IV	1046.313	-0.44	390247.987	-4.28 ± 0.54	FUSE
	1080.967	0.53	501509.203	-4.15 ± 0.45	
	1080.969	0.68	501564.414	...	
	1080.970	0.47	501509.203	...	
	1080.970	0.62	501564.414	...	
	1081.024	-0.94	390161.195	...	
	1338.615	-0.63	180480.794	-4.24 ± 0.20	G130M
	1342.990	-1.33	180724.206		
	1343.514	-0.38	180724.206		
O V	1371.296	-0.33	158797.700	-4.21 ± 0.25	

NOTE—Abundance relative to hydrogen: $\log N(X)/N(\text{H})$.^aMultiplet.**Table A2.** Additional Absorption Features

Ion	λ_{lab} (\AA)	$\log gf$	E_l (cm^{-1})	Abundance	Grating
Si IV	1066.614	0.72	160374.406	-5.17 ± 0.32	FUSE
	1066.636	-0.59	160374.406	...	
	1066.650	0.56	160375.589	...	
	1128.325	-0.48	71748.643	-5.61 ± 0.28	
	1128.340	0.47	71748.643	...	
	1393.755	0.03	0.000	-5.11 ± 0.18	G130M
	1402.770	-0.28	0.000	-5.29 ± 0.21	
P IV	1030.514	-0.44	68146.475	-7.29 ± 0.18	FUSE
	1030.515	0.25	68615.174	...	
	1033.112	-0.32	68146.475	-7.06 ± 0.28	
P V	1117.977	-0.01	0.000	-6.77 ± 0.17	
	1128.008	-0.32	0.000	-6.85 ± 0.18	

Table A2 *continued*

Table A2 (*continued*)

Ion	λ_{lab} (Å)	$\log gf$	E_t (cm^{-1})	Abundance	Grating
S IV	1062.678	-1.09	0.000	-5.09 ± 0.42	FUSE
	1072.996	-0.83	951.100	-5.92 ± 0.23	
	1073.528	-1.79	951.100	...	
	1098.357	-1.75	94103.097	-5.77 ± 0.20	
	1098.917	-0.61	94150.403	...	
	1099.472	-0.80	94103.097	...	
S V	1122.042	0.09	234956.003	-5.27 ± 0.17	
	1128.667	-0.07	234947.098	...	
	1128.776	-0.97	234956.003	...	
	1268.493	-0.30	270700.417	-5.57 ± 0.35	G130M
	1501.760	-0.50	127150.700	-5.31 ± 0.44	G160M
Fe V	1406-1412 ^a	-5.22 ± 0.25	G160M
	1413-1418 ^a	-5.38 ± 0.27	
	1419-1421 ^a	-5.39 ± 0.22	
	1428-1431 ^{a,b}	-5.31 ± 0.25	
	1440-1450 ^a	-5.50 ± 0.30	
	1450-1460 ^a	-5.60 ± 0.34	
	1460-1470 ^a	-5.53 ± 0.29	
	1470-1480 ^a	-5.38 ± 0.36	
1531-1534 ^{a,b}	-5.23 ± 0.26		
Ni IV	1398.193	0.58	110410.598	-6.69 ± 0.35	G130M
	1411.451	0.45	111195.796	-6.36 ± 0.26	
	1411.451	0.45	111195.796	-6.47 ± 0.30	G160M
	1452.220	0.70	139289.405	-6.32 ± 0.43	
	1493.672	0.70	155253.703	-6.77 ± 0.93	
Ni V	1265-1268 ^b	-6.44 ± 0.39	G130M
	1276.958	0.17	164525.901	-6.75 ± 0.70	
	1307.603	0.17	178019.794	-6.50 ± 0.25	
	1313.280	0.30	208163.695	-6.34 ± 0.73	

NOTE—Abundance relative to hydrogen: $\log N(\text{X})/N(\text{H})$.

^aSpectral region with multiple features. See discussion in text.

^bRegion includes Fe IV features.

REFERENCES

- Asplund, M., Grevesse, N., Sauval, A. J., & Scott, P. 2009, *ARA&A*, 47, 481, doi: [10.1146/annurev.astro.46.060407.145222](https://doi.org/10.1146/annurev.astro.46.060407.145222)
- Baumgardt, H., & Vasiliev, E. 2021, *MNRAS*, 505, 5957, doi: [10.1093/mnras/stab1474](https://doi.org/10.1093/mnras/stab1474)
- Chayer, P., Dixon, W. V., Fullerton, A. W., Ooghe-Tabanou, B., & Reid, I. N. 2015, *MNRAS*, 452, 2292, doi: [10.1093/mnras/stv1435](https://doi.org/10.1093/mnras/stv1435)
- Clausen, D., & Wade, R. A. 2011, *ApJL*, 733, L42, doi: [10.1088/2041-8205/733/2/L42](https://doi.org/10.1088/2041-8205/733/2/L42)
- Cox, A. N. 2000, *Allen's Astrophysical Quantities* (New York: Springer-Verlag), <https://ui.adsabs.harvard.edu/abs/2000asqu.book....1C>
- Crestani, J., Alves-Brito, A., Bono, G., Puls, A. A., & Alonso-García, J. 2019, *MNRAS*, 487, 5463, doi: [10.1093/mnras/stz1674](https://doi.org/10.1093/mnras/stz1674)
- Debes, J., Sankrit, R., Fischer, T., et al. 2024, *The Hubble Advanced Spectral Product (HASP) Program, Instrument Science Report COS 2024-01*, <https://ui.adsabs.harvard.edu/abs/2024cos..rept....1D>
- Dixon, W. V. 2024, *AJ*, 167, 47, doi: [10.3847/1538-3881/ad11e0](https://doi.org/10.3847/1538-3881/ad11e0)
- Dixon, W. V., Chayer, P., Latour, M., Miller Bertolami, M. M., & Benjamin, R. A. 2017, *AJ*, 154, 126, doi: [10.3847/1538-3881/aa8450](https://doi.org/10.3847/1538-3881/aa8450)
- Dixon, W. V., Sahnou, D. J., Barrett, P. E., et al. 2007, *PASP*, 119, 527, doi: [10.1086/518617](https://doi.org/10.1086/518617)
- Fitzpatrick, E. L. 1999, *PASP*, 111, 63, doi: [10.1086/316293](https://doi.org/10.1086/316293)
- Flower, P. J. 1996, *ApJ*, 469, 355, doi: [10.1086/177785](https://doi.org/10.1086/177785)
- Gaia Collaboration, Prusti, T., de Bruijne, J. H. J., et al. 2016, *A&A*, 595, A1, doi: [10.1051/0004-6361/201629272](https://doi.org/10.1051/0004-6361/201629272)
- Gaia Collaboration, Brown, A. G. A., Vallenari, A., et al. 2021, *A&A*, 649, A1, doi: [10.1051/0004-6361/202039657](https://doi.org/10.1051/0004-6361/202039657)
- Gaia Collaboration, Vallenari, A., Brown, A. G. A., et al. 2023, *A&A*, 674, A1, doi: [10.1051/0004-6361/202243940](https://doi.org/10.1051/0004-6361/202243940)
- Gerber, J. M., Briley, M. M., & Smith, G. H. 2019, *AJ*, 157, 154, doi: [10.3847/1538-3881/ab0b3f](https://doi.org/10.3847/1538-3881/ab0b3f)
- Gontcharov, G. A., Khovritchev, M. Y., Mosenkov, A. V., et al. 2023, *MNRAS*, 518, 3036, doi: [10.1093/mnras/stac3300](https://doi.org/10.1093/mnras/stac3300)
- Gratton, R. G., Lucatello, S., Sollima, A., et al. 2015, *A&A*, 573, A92, doi: [10.1051/0004-6361/201424393](https://doi.org/10.1051/0004-6361/201424393)
- Green, J. C., Froning, C. S., Osterman, S., et al. 2012, *ApJ*, 744, 60, doi: [10.1088/0004-637X/744/1/60](https://doi.org/10.1088/0004-637X/744/1/60)
- Guerrero, M. A., & De Marco, O. 2013, *A&A*, 553, A126, doi: [10.1051/0004-6361/201220623](https://doi.org/10.1051/0004-6361/201220623)
- Harris, W. E. 1996, *AJ*, 112, 1487, doi: [10.1086/118116](https://doi.org/10.1086/118116)
- . 2010, *arXiv e-prints*. <https://arxiv.org/abs/1012.3224>
- Heber, U. 2016, *PASP*, 128, 082001, doi: [10.1088/1538-3873/128/966/082001](https://doi.org/10.1088/1538-3873/128/966/082001)
- Hubeny, I. 1988, *CoPhC*, 52, 103, doi: [10.1016/0010-4655\(88\)90177-4](https://doi.org/10.1016/0010-4655(88)90177-4)
- Hubeny, I., & Lanz, T. 1995, *ApJ*, 439, 875, doi: [10.1086/175226](https://doi.org/10.1086/175226)
- Kalirai, J. S., Davis, D. S., Richer, H. B., et al. 2009, *ApJ*, 705, 408, doi: [10.1088/0004-637X/705/1/408](https://doi.org/10.1088/0004-637X/705/1/408)
- Kurucz, R. L. 1979, *ApJS*, 40, 1, doi: [10.1086/190589](https://doi.org/10.1086/190589)
- Lanz, T., & Hubeny, I. 2003, *ApJS*, 146, 417, doi: [10.1086/374373](https://doi.org/10.1086/374373)
- Latour, M., Fontaine, G., Green, E. M., & Brassard, P. 2015, *A&A*, 579, A39, doi: [10.1051/0004-6361/201525999](https://doi.org/10.1051/0004-6361/201525999)
- Latour, M., Randall, S. K., Chayer, P., et al. 2017, *A&A*, 600, A130, doi: [10.1051/0004-6361/201630132](https://doi.org/10.1051/0004-6361/201630132)
- Lehner, N., Howk, J. C., Thom, C., et al. 2012, *MNRAS*, 424, 2896, doi: [10.1111/j.1365-2966.2012.21428.x](https://doi.org/10.1111/j.1365-2966.2012.21428.x)
- Luo, A. L., Zhao, Y. H., Zhao, G., & et al. 2022, *VizieR Online Data Catalog: LAMOST DR7 catalogs, V/156*, <https://ui.adsabs.harvard.edu/abs/2022yCat.5156....0L>
- Luo, Y., Németh, P., Wang, K., & Pan, Y. 2024, *ApJS*, 271, 21, doi: [10.3847/1538-4365/ad1ab2](https://doi.org/10.3847/1538-4365/ad1ab2)
- Menzies, J. 1974, *MNRAS*, 168, 177, doi: [10.1093/mnras/168.1.177](https://doi.org/10.1093/mnras/168.1.177)
- Michaud, G., Alecian, G., & Richer, J. 2015, *Atomic Diffusion in Stars* (Cham: Springer), doi: [10.1007/978-3-319-19854-5](https://doi.org/10.1007/978-3-319-19854-5)
- Miller Bertolami, M. M. 2016, *A&A*, 588, A25, doi: [10.1051/0004-6361/201526577](https://doi.org/10.1051/0004-6361/201526577)
- Moehler, S., Landsman, W., & Napiwotzki, R. 1998, *A&A*, 335, 510, doi: [10.48550/arXiv.astro-ph/9803313](https://doi.org/10.48550/arXiv.astro-ph/9803313)
- Moehler, S., Landsman, W. B., Lanz, T., & Miller Bertolami, M. M. 2019, *A&A*, 627, A34, doi: [10.1051/0004-6361/201935694](https://doi.org/10.1051/0004-6361/201935694)
- Moos, H. W., Cash, W. C., Cowie, L. L., et al. 2000, *ApJL*, 538, L1, doi: [10.1086/312795](https://doi.org/10.1086/312795)
- Morton, D. C. 2003, *ApJS*, 149, 205, doi: [10.1086/377639](https://doi.org/10.1086/377639)
- Napiwotzki, R., Barstow, M. A., Fleming, T., et al. 1993, *A&A*, 278, 478, <https://ui.adsabs.harvard.edu/abs/1993A&A...278..478N>
- Németh, P., Kawka, A., & Vennes, S. 2012, *MNRAS*, 427, 2180, doi: [10.1111/j.1365-2966.2012.22009.x](https://doi.org/10.1111/j.1365-2966.2012.22009.x)
- Planck Collaboration, Abergel, A., Ade, P. A. R., et al. 2014, *A&A*, 571, A11, doi: [10.1051/0004-6361/201323195](https://doi.org/10.1051/0004-6361/201323195)
- Press, W. H., Flannery, B. P., Teukolsky, S. A., & Vetterling, W. T. 1989, *Numerical recipes in C. The art of scientific computing* (Cambridge University Press), <https://ui.adsabs.harvard.edu/abs/1989nrca.book....P>

- Riello, M., De Angeli, F., Evans, D. W., et al. 2021, *A&A*, 649, A3, doi: [10.1051/0004-6361/202039587](https://doi.org/10.1051/0004-6361/202039587)
- Rojas-Arriagada, A., Zoccali, M., Vásquez, S., et al. 2016, *A&A*, 587, A95, doi: [10.1051/0004-6361/201527351](https://doi.org/10.1051/0004-6361/201527351)
- Sahnow, D. J., Moos, H. W., Ake, T. B., et al. 2000, *ApJL*, 538, L7, doi: [10.1086/312794](https://doi.org/10.1086/312794)

- Torres, G. 2010, *AJ*, 140, 1158, doi: [10.1088/0004-6256/140/5/1158](https://doi.org/10.1088/0004-6256/140/5/1158)
- Vasiliev, E., & Baumgardt, H. 2021, *MNRAS*, 505, 5978, doi: [10.1093/mnras/stab1475](https://doi.org/10.1093/mnras/stab1475)
- Webbink, R. F. 1984, *ApJ*, 277, 355, doi: [10.1086/161701](https://doi.org/10.1086/161701)
- Werner, K., Dreizler, S., Heber, U., et al. 1996, *A&A*, 307, 860, <https://ui.adsabs.harvard.edu/abs/1996A&A...307..860W>